Phase equilibrium experiments and thermodynamic simulations to constrain the pre-eruptive conditions of the 2021 Tajogaite eruption (Cumbre Vieja volcano, La Palma, Canary Islands)

Alessandro Fabbrizio[a,*], Emily C. Bamber[b], Eleni Michailidou[a], Jorge E. Romero[c,d], Fabio Arzilli[e], Barbara Bonechi[d], Margherita Polacci[d], Mike Burton[d]

[a]*Institute of Petrology and Structural Geology, Faculty of Science, Charles University, Albertov 6, 128 43 Prague, Czech Republic*

[b]*Department of Earth Sciences, University of Turin, Via Valperga Caluso, 35, 10125, Turin, Italy*

[c]*Instituto de Ciencias de la Ingeniería, Universidad de O'Higgins, Libertador Bernardo O'Higgins 611, Rancagua, Chile*

[d]*Department of Earth and Environmental Sciences, The University of Manchester, Manchester M13 9PL, United Kingdom*

[e]*School of Science and Technology, Geology Division, University of Camerino, Camerino, Italy*

[*]Corresponding author.

*Email addres*s: alessandro.fabbrizio@natur.cuni.cz (A. Fabbrizio).

Abstract

Phase relations of a tephritic lava erupted at La Palma, Canary Islands, the 2nd of October 2021, during the eruption of Cumbre Vieja volcano were determined experimentally in the temperature/water content space, *T* (°C)/H_2O (wt%). The crystallisation experiments were carried out at a fixed pressure of 275 MPa for temperatures varying from 1000 to 1200 °C and with H_2O added contents ranging from 0 to 5 wt%. Results from the synthetic products are compared with those obtained from thermodynamic simulations and with the natural phases to constrain the pre-eruptive conditions of the tephritic magma stored in the shallow reservoir. The major phases (clinopyroxene + olivine + oxides) occurring in the natural products were reproduced. The experimental results combined with thermodynamic modelling allow us to constrain the pre-eruptive temperature to ~1100 °C considering H_2O to 3 wt% and to restrict the crystallisation of plagioclase at low pressures (< 20 MPa). The results indicate that, under the presence of a pure H_2O fluid, amphibole is stable at pressures higher than 300 MPa and temperatures ~1000 °C. Our results on pre-eruptive conditions of the 2021 Tajogaite eruption provide important constraints on mechanisms of storage and transport in primitive alkaline magmas.

Keywords:

phase equilibrium experiments; thermodynamic simulations; undercooling; crystallisation; pre-eruptive conditions; Cumbre Vieja

1. Introduction

This experimental study focuses on the physical parametrization of the recent eruption which happened in La Palma, one of the most historically active volcanic islands of the Canarian Archipelago. Particularly, we aim to constrain the pre-eruptive conditions of the 2021 Cumbre Vieja eruption (Tajogaite volcano, La Palma, Canary Islands) that began on 19 September 2021 after 40 years of quiescence and ended on 13 December 2021. Seismicity during the eruption indicates magma intrusions at 8-12 and 20-25 km depth (D'Auria et al., 2022). The erupted rocks are tephritic-basanitic in composition (Carracedo et al., 2022; Castro and Feisel, 2022; Day et al., 2022; Dayton et al., 2023; Di Fiore et al., 2023; Pankhurst et al., 2022; Romero et al., 2022; Ubide et al., 2023). Over the course of three months, the Tajogaite volcano displayed hybrid volcanic activity consisting of effusive phases with emission of lava flows, explosive phases with pyroclastic columns reaching 8500 m asl (PEVOLCA, 2021), with resulting ash-falls spread all over La Palma, and intense degassing from different simultaneously active craters (Bonadonna et al., 2022; Martínez-Martínez et al., 2023).

Previous works have examined magma migration from the mantle to the surface, the pressure-temperature conditions that produced exceptionally fast and fluid lava at high discharge rates, the eruptive dynamics and cone collapse, the depths of magma storage, the geochemical variations over the entire eruptive period, and the effects of the eruption on La Palma infrastructure and inhabitants (Bonadonna et

al., 2022; Carracedo et al., 2022; Castro and Feisel, 2022; Day et al., 2022; Dayton et al., 2023; Padron et al., 2022; Romero et al., 2022; Di Fiore et al., 2023; Ubide et al., 2023). However, an experimental constraint of the pre-eruptive conditions within the Cumbre Vieja plumbing system is still lacking.

In this study, phase equilibria for tephritic magma were determined at fixed pressure in the *T*-H_2O wt% space by laboratory experiments and thermodynamic modelling to define the pre-eruptive conditions of the 2021 Cumbre Vieja eruption.

The Canary Islands represent, after Hawaii, the most important example of hot spot related volcanism (Cas et al., 2022) and its volcanoes are among the most active on Earth, as shown by the recent eruptions of El Hierro (2011-2012) and Cumbre Vieja (2021).

Mantle plume-related magmatism (hot spot zones) in intracontinental settings and oceanic environments may produce either short-lived voluminous eruptions of basaltic magmas or build an oceanic island volcano (e.g. Houghton and Gonnermann, 2008; Caracciolo et al., 2021; Cas et al., 2022). Mantle plumes can produce a relatively large amount of magma, which can migrate from the mantle to the surface. The pressure and temperature conditions controlling magma storage within the crust and magma eruptability in plume-related volcanism have been investigated in previous studies (e.g. Klugel et al., 2005; Haddadi et al., 2017; Oglialoro et al., 2017; Padron et al., 2022), where the pre- and syn-eruptive conditions were constrained by mineral-melt thermobarometry, melt and fluid inclusions (e.g. Hildner et al., 2012;

Bali et al., 2018; Hartley et al., 2018). However, phase equilibrium studies to constrain the pre-eruptive conditions of this style of volcanism are still scarce (Martí et al., 2013).

Previous phase equilibrium studies which determined the pre-eruptive conditions for a series of eruptions of the Canary Islands include: Abrigo 190 kyr ago (Andújar et al., 2008); Montaña Blanca 2020 y.b.p. (Fabbrizio et al., 2006; Andújar and Scaillet, 2012); Teide-Pico Viejo 1800 y.b.p. (Andújar et al., 2013); Teide 1150 y.b.p. (Andújar et al., 2010), El Hierro 2011-2012 (Martí et al., 2013). All these studies, with the exception of Martí et al. (2013), investigated phase equilibria for phonolitic compositions, constraining the pre-eruptive storage of magma at relatively shallow depths (≤ 150 MPa) and temperatures lower than 900 °C. Martí et al. (2013) performed a phase equilibrium study, combined with mineral-melt geothermometry and thermodynamic modelling, for basanitic compositions at a fixed pressure of 400 MPa, constraining the pre-eruptive temperature in the range of 1100-1185 °C.

Given magma reservoirs are inaccessible, the synthetic reproduction of natural phase compositions and assemblages using crystallisation experiments allows us to constrain intensive parameters such as temperature, pressure, oxygen fugacity and volatile content. Therefore, we can characterize the conditions of magmas before eruptions. Equilibrium experiments are also used to obtain phase diagrams in which mineral phases' stability fields are constrained as a function of pressure (P), temperature (T) conditions, water content (H_2O

wt%) and/or mixed fluid (XH$_2$O). Therefore, equilibrium crystallisation experiments help to reproduce the mineral assemblage, chemical compositions of the phases and textures of erupted products. The comparison between the chemistry and the texture of the run products with those of the natural samples allows the pre-eruptive conditions of the volcanic system to be defined. This kind of study is critical in order to better understand the behavior of explosive eruptions given the profound economic and societal consequences such eruptions can produce (Blundy and Cashman, 2008). Moreover, experimental petrology data for understudied magmatic systems are pivotal to improve the accuracy of mineral-melt thermobarometry. In turn, the experimentally derived pre-eruptive conditions can help risk-managers and decision-makers improve volcano monitoring and disaster mitigation systems.

2. Experimental and analytical methods

2.1. Strategy

We performed equilibrium crystallisation experiments using tephritic compositions, which represent the most common compositions erupted during the first three weeks of the 2021 Cumbre Vieja eruption (Day et al., 2022). Most of the reported experiments were performed under hydrous conditions with 1, 3 and 5 wt% H_2O added. The experiments were run with different water contents to test the stability

fields of the mineral phases. The experimental pressure was fixed to 275 MPa to simulate equilibrium crystallisation in the shallow magmatic reservoir located at a depth of 8-12 km (D'Auria et al., 2022).

2.2. Starting materials

The tephritic natural starting material (CVLP-LF3, Table 1) was erupted on 2 October 2021 and collected the day after during a field campaign carried out between 20 September and 20 October 2021 (Romero et al., 2022), hence representing some of the products erupted in the initial phase of the event. The sample is glassy, highly vesiculated and contains phenocrysts of clinopyroxene, Fe-Ti oxides, olivine and plagioclase microlites. Using this sample, one anhydrous and two hydrous (with 1 and 3 wt% H_2O added) starting materials were prepared.

The anhydrous starting material was created by grinding, in an agate mortar under ethanol, a few grams of the tephrite (CVLP-LF3; Romero et al., 2022) into a fine homogenous powder. A hydrous-rich (5 wt% H_2O added, Table 1) starting material, representing a synthetic mixture analogue to the composition of the natural tephrite, was obtained by mixing a total of 1 g of oxides (SiO_2, TiO_2, Al_2O_3, FeO, MgO, MnO), hydroxides ($Al(OH)_3$), silicates ($CaSiO_3$, Na_2SiO_3, K_2SiO_3) and phosphate ($Ca_5(OH)(PO_4)_3$) in appropriate proportions. All chemical compounds were new and when opened were stored at 110 °C prior to weighing and mixing. All powders were homogenized in an agate mortar under ethanol. A suite of trace elements (Li, Rb, Cs, Co,

Cu, Zn, Sr, Cd, Ba, Pb, Sc, Cr, Ga, Y, La, Ce, Pr, Nd, Sm, Eu, Gd, Tb, Dy, Ho, Er, Tm, Yb, Lu, Ge, Zr, Sn, Hf) were added to the anhydrous and to the hydrous-rich starting mixtures as oxides or chlorides in an amount totalling 1 wt%, resulting in individual trace elements concentrations of ~200 to 300 ppm. These mixtures were re-ground under ethanol after each addition.

The other hydrous starting materials (1 and 3 wt% H_2O added) were created by mixing in appropriate amounts, in an agate mortar under ethanol, the natural anhydrous composition with the hydrous-rich synthetic analogue. All prepared starting materials (Table 1) were stored, prior to their encapsulation, in a furnace at 110 °C to prevent water and CO_2 adsorption.

2.3. Quickpress experiments

The experiments (Table 2) were carried out at the Experimental Petrology Laboratory of the Institute of Petrology and Structural Geology (Charles University) in a Quickpress non-endloaded piston cylinder apparatus at 275 MPa in the temperature range 1000 to 1200 °C. Approximately 20 mg of the starting powders were loaded into cylindrical $Au_{80}Pd_{20}$-capsules (OD: 3 mm, ID: 2.7 mm). Capsules were sealed by arc-welding under a flux of argon that cooled them. The employed 19-25 mm NaCl-pyrex-graphite-MgO low-pressure assemblies impose relatively oxidizing conditions at about 2-log units above the Ni-NiO buffer (Masotta et al., 2012). Temperature was

measured by factory-calibrated S-type (Pt-$Pt_{90}Rh_{10}$) thermocouples with an accuracy of ±2 °C. Runs were cold-pressurized to a pressure 10% higher than the target value, then the pressure was decreased down to 275 MPa. No correction was applied for the pressure effects on e.m.f. Experiments were first heated at a rate of 15 °C/min to 700 °C to allow a gently dissociation of $Al(OH)_3$, then raised to 1200 °C (superliquidus) with a rate of 50 °C/min. The superliquidus temperature was maintained for 1 hour to allow melt homogenization and then decreased to the target temperature at a cooling rate of 60 °C/h. Run duration at the final temperature ≥ 1100 °C was 24 hours and 48 hours below 1100 °C. One reversal experiment, here the term reversal is used to indicate runs that were performed with a different thermal/temporal history compared to the one described above, was performed by keeping it at 1100 °C for 48 hours after cooling from superliquidus temperature. A second reversal experiment was performed by heating the assembly directly from room temperature to 1100 °C and keeping the temperature constant for 24 hours. The advantage of heating the experimental charge at superliquidus temperature and then cooling it at target temperature is that resting at superliquidus temperature promotes chemical homogeneity of the melt (by melting of all residual crystal nuclei in the case of a natural-rock powder or by complete reaction of the chemical compounds in the case of a synthetic starting material) from which few and large crystals will precipitate once the run is at target temperature. On the other hand, the direct heating of the experimental charge from room to target temperature does not guarantee reaching chemical

homogeneity before crystallisation begins because of the presence of residual crystal nuclei or incomplete reaction of the chemical compounds. Moreover, experimental charges heated directly to final temperature will be characterized by a large number of crystals with small size (nucleation enhanced versus growth) compared to the textures obtained from the experiments cooled from superliquidus temperature (growth enhanced versus nucleation). Consequently, a good agreement between the mineralogical assemblage and the chemistry of the phases obtained in runs performed with these different strategies can be considered as a proof that equilibrium, or at least near-equilibrium, conditions were attained. All experiments were terminated by switching off the power, resulting in a cooling rate >100 °C/s. Pressure was kept constant during quench. The recovered capsules were mounted in epoxy and polished for analysis.

2.4. Analytical techniques

Back-scattered electron images (BSE) of the samples and the major and minor component concentrations of run products were obtained using the JEOL JXA-8530F Electron Microprobe Analyzer (EMPA) at the Institute of Petrology and Structural Geology, Charles University. Analytical conditions for mineral phases were 15 kV, 10 nA beam current, 1 μm beam size and counting times of 20 s for all elements with half-time on background. Glasses were analyzed under the same conditions with the exception of the beam size that was set to

10 μm. Alkalis (Na, K) were analyzed first in order to minimize their loss during glass analyses. Measurement errors based on counting statistics were <10% for all elements in all phases. The following standards were used for calibration: quartz (Si), corundum (Al), rutile (Ti), chromium oxide (Cr), vanadinite (V), magnetite (Fe), periclase (Mg), rhodonite (Mn), calcite (Ca), albite (Na), sanidine (K), apatite (P), topaz (F), halite (Cl). The ZAF correction was used to perform the data reduction. The analyses for minerals and glasses as well as BSE images of the experimental charges are presented in Supplementary Table 1.

3. Results

3.1. Phase equilibria

BSE images of all experiments are shown in Supplementary Table 1 and a selection of them is shown in Fig. 1. Experimental results are reported in Table 2. The attainment of equilibrium is indicated by the homogenous distribution of phases in all experimental charges and the run duration (24 h at 1100-1200 °C; 48 h at 1000-1050 °C), which is similar to those of previous phase equilibrium studies on basaltic systems (e.g., Arzilli et al., 2015; La Spina et al., 2016; Polacci et al., 2018). As a comparison, one day at 1060 °C/1 atm was found to be sufficient for an andesite to reach a steady state with respect to the melt composition and phase assemblage (Baker and Eggler, 1987). Additional evidence which indicates the attainment of equilibrium in the

experiments includes the euhedral shapes of mineral phases and the close correspondence in both texture and composition between the three experiments performed at 1100 °C/1 wt% H_2O with different temporal and thermal strategies (i.e., resting at 1100 °C for 24 and 48 h after cooling from 1200 °C; direct heating to 1100 °C and resting for 24 h).

The experimental results (Fig. 2) highlight that with up to 1 wt% water added, olivine crystallises between 1150 and 1175 °C, followed by clinopyroxene between 1100 and 1125 °C. With increasing water content, the appearance of olivine is lowered to 1100-1125 °C (3 wt% H_2O) and <1000 °C (5 wt% H_2O). Instead, the appearance of clinopyroxene is not affected by the water content (0-5 wt% H_2O), which is always in the temperature interval 1100-1125 °C. The crystallisation temperatures of oxides (Cr-spinel and Ti-magnetite) are strongly influenced by the water content, decreasing for Cr-spinel from ~1200 °C at anhydrous conditions to ~1125 °C with 3 wt% water added and for Ti-magnetite decreasing from ~1100 to ~1000 °C, respectively, with 5 and 1 wt% H_2O added. Amphibole and apatite were only found at 1000 °C/1 wt% H_2O.

3.2. Description of the experimental charges

The experimental runs (1 wt% H_2O) performed at temperatures equal to or higher than 1175 °C are superliquidus, as well as those with 3 and 5 wt% H_2O added at temperatures of 1150 °C and equal or higher than 1125 °C, respectively (Supplementary Table 1; Fig. 2). The first

phase to appear is oxide, as Cr-spinel (Cr-sp; 0 wt % H_2O/1175 °C, 1 wt% H_2O/1150 °C, 3 wt% H_2O/1125 °C) or Ti-magnetite (Ti-mt; 5 wt% H_2O/1150 °C). Oxides are mostly euhedral, with sizes between 5-10 μm for Cr-spinel and 30-40 μm for Ti-magnetite (Fig. 1; Supplementary Table 1). Cr-spinel and Ti-magnetite never coexist in the same experimental charge (see section 4.1 for a detailed explanation).

Olivine is present in the experimental charges with up to 3 wt% H_2O added. The shape of olivine crystals changes as a function of the degree of undercooling (i.e., ΔT, the temperature difference between the liquidus temperature of the specific mineral phase and its crystallisation temperature; Kirkpatrick, 1981), as already observed in previous experimental studies (Faure et al., 2003; Faure et al., 2007; Lang et al., 2021). In experimental runs performed at a low degree of undercooling (i.e., ΔT= ~12 °C, runs at 0 wt% H_2O/1150 °C, 1 wt% H_2O/1150 °C, 3 wt% H_2O/1100 °C), olivine is euhedral, with a size ranging from 30 to 100 μm. At higher degrees of undercooling (ΔT= ~37 °C) and a temperature of 1125 °C, olivine crystals are mostly euhedral with some crystals hosting a melt pocket (0 wt% H_2O/1125 °C). As the degree of undercooling increases (ΔT= ~62 °C) in the runs performed at 1100 °C with up to 1 wt% H_2O added, olivine crystals are mostly skeletal with embayments, hosting one or multiple melt pockets, although rare euhedral crystals are still present (Fig. 1; Supplementary Table 1). The reversal run performed at 1100 °C for 48 h after cooling from 1200 °C is characterized by olivine crystals that are mostly euhedral (some hosting a melt pocket). The run heated directly to 1100 °C shows only euhedral

olivine crystals, suggesting that the skeletal shapes are a direct consequence of the degree of undercooling and of the experimental time spent at the final temperature. At the lowest temperature, i.e., 1000 °C/highest degree of undercooling (ΔT= ~162 °C), olivine crystals show only skeletal shapes (Shea et al., 2019).

Clinopyroxene appears in all runs performed at or below 1100 °C. At 1100 °C crystals are euhedral with zones enriched in Si-Mg (darker areas in the BSE images) and in Ti-Al (brighter areas in the BSE images) and with sizes exceeding 100 μm, occasionally hosting a melt pocket (Fig. 1; Supplementary Table 1). The different zones enriched in Si-Mg and Ti-Al have already been observed in clinopyroxene crystals crystallising from undercooled melts (Colle et al., 2023; Masotta et al., 2020; Moschini et al., 2021; MacDonald et al., 2022). In the runs performed at 1000 and 1050 °C clinopyroxene crystals are mostly euhedral, and they host multiple melt pockets or they are characterized by the presence of embayments (Supplementary Table 1). Rare euhedral crystals of amphibole (15-30 μm wide) and apatite (<15 μm wide) crystallised in the run performed at 1000 °C with 1 wt% H_2O added (Supplementary Table 1).

3.3. Phase compositions

The chemical compositions of the residual glasses (representative of the residual melt compositions produced by crystallisation, Fig. 3), clinopyroxene, olivine, Cr-spinel, Ti-magnetite,

apatite, and amphibole are reported in Supplementary Table 1. The compositions of the residual melts change according to the phase equilibria. The apparent low total of the anhydrous glasses (95-97 wt%) are due either to trace elements (1 wt%) not measured during analysis and to their increased concentration (>1 wt%) in the residual melts with progressing crystallisation, either to small or negligible hygroscopic water absorption during capsule preparation or hydrogen diffusion into the capsule during the run (Fabbrizio et al., 2021), or either to element migration and redox changes caused by sub-surface charging effects during analysis (1 wt%; Hughes et al., 2019). The combination of these effects suggest negligible or no water contamination of the anhydrous glasses. The SiO_2 contents start to increase noticeably with the initiation of clinopyroxene crystallisation between 1100 and 1125 °C. The trend in Al_2O_3 content as a function of temperature is also similar to that of SiO_2. In correspondence with the onset of clinopyroxene crystallisation, CaO contents start to decrease with its appearance below 1125 °C. Considering all the experiments performed in this study, the MgO content of residual glasses decreases as a result of oxides, olivine and clinopyroxene crystallisation. The compositions of residual glasses indicate that FeO trends are not affected by Cr-spinel and olivine crystallisation, as their FeO concentrations tend to decrease markedly only after the appearance of clinopyroxene and of Ti-magnetite. The low FeO content in the residual glass at 1125 °C with 5 wt% H_2O may suggest some iron loss during this run. TiO_2 can be considered roughly constant in all glasses given that it decreases markedly only after the

appearance of Ti-magnetite. MnO contents tend to increase with decreasing temperature, reach a maximum at 1100 °C and then decrease abruptly at lower temperature with the appearance of Ti-magnetite. Alkalis (i.e., Na_2O and K_2O) increase markedly with the appearance of clinopyroxene. P_2O_5 contents increase steadily with the appearance of clinopyroxene, the crystallisation of apatite at 1000 °C in the run with 1 wt% H_2O buffers its increase.

The forsterite contents of experimental olivine vary between Fo_{82} and Fo_{87} as a function of the experimental temperature (Fig. 4). Clinopyroxene in the experimental charges shows a fairly constant diopsidic composition with temperature, ranging from $Wo_{46}En_{47}Fs_8$ to $Wo_{52}En_{32}Fs_{16}$ (Fig. 4). Oxides (Cr-spinel) and apatite were difficult to analyze due to their small size, but analyses free of contamination from other phases are reported in Supplementary Table 1. Ti-rich kaersetutic (6 wt% TiO_2) amphibole (Supplementary Table 1) only crystallised at 1000 °C in the charge with 1 wt% H_2O added.

4. Discussion

In the following sections we will compare the experimental results with the natural erupted products and with crystallisation simulations performed by MELTS. We will use the experimental and thermodynamic results to infer the pre-eruptive temperature and water contents of the magma stored in the shallow reservoir at a corresponding pressure of 275 MPa (D'Auria et al., 2022).

4.1. Comparison with the natural erupted rocks

Comparing the experimental results with the natural lava and tephra (Castro and Feisel 2022; Day et al., 2022; Pankhurst et al., 2022; Romero et al., 2022) we observe that the natural phase assemblage of clinopyroxene, olivine and oxides is well reproduced in terms of mineral phase composition and texture by the experiments performed at 1100 °C with up to 3 wt% H_2O added. This water content is comparable with previous estimations of H_2O content for historical erupted products of Cumbre Vieja (Weis et al., 2015) and for oceanic island basalts (Kovalenko et al., 2007) as well as with the melt H_2O content (0.8 wt%, plagioclase-liquid hygrometer) determined by pairs of plagioclase microlites and matrix glass for the erupted tephra of the 2021 eruption of Cumbre Vieja (Castro and Feisel 2022). The above water content is also in agreement with the melt water contents estimated for undegassed Canary magmas (Longpré et al., 2017; Walowski et al., 2017; Taracsak et al., 2019).

Experimental clinopyroxene (Figs. 4, 5), is the most abundant phase, with euhedral crystals characterized by sector zoning, the observed compositions are in a quite narrow range from $Wo_{46}En_{47}Fs_{8}$ to $Wo_{52}En_{32}Fs_{16}$, reproducing well the clinopyroxene compositions (Wo_{47} $En_{40}Fs_{13}$-$Wo_{51}En_{33}Fs_{16}$) of the natural tephra and lava (Castro and Feisel 2022; Day et al., 2022; Pankhurst et al., 2022; Romero et al., 2022).

The experimental olivine (Fig. 4) compositions range from Fo_{82} to Fo_{87}, comparable to those of natural olivine crystals (Fo_{78}-Fo_{86}) as

well as skeletal and rounded-embayed shapes similar to those observed in the natural samples (Day et al., 2022; Pankhurst et al., 2022; Dayton et al., 2023).

The presence of Ti-magnetite in the runs with 5 wt% H_2O added as well as in the high-crystalline run performed at 1000 °C/1 wt% H_2O coupled with the absence of Cr-spinel in the runs performed at higher water contents suggests that oxide stability is influenced by the degree of evolution of the residual melt from where it precipitates. Ti-magnetite is associated with more evolved melts whereas Cr-spinel crystallises in more primitive melts. This experimental evidence is corroborated by the observation that Ti-magnetite is found in the earliest and more evolved erupted lavas, which have compositions that extend to phonotephrite (Day et al., 2022). Moreover, the less evolved erupted lavas have higher Cr_2O_3 contents than the more evolved ones, thus favoring the crystallisation of Cr-spinel (Day et al., 2022).

Hydrous phases such as amphibole and apatite are present only in the run at 1000 °C/1 wt% H_2O suggesting that their crystallisation was related to a relative increase of the water content in the residual melt due to the high crystallinity of this experimental charge. The natural products erupted between 19-27 September show kaersutitic amphibole crystals with evident reaction rims (Day et al., 2022; Pankhurst et al., 2022; Romero et al., 2022; Ubide et al., 2023) suggesting that amphibole was outside of its stability field during the ascent and storage of magma at a shallow depth within the crust. The lack of amphibole crystals in the experimental charges could imply that

amphibole crystallised from a hotter and more primitive magma at pressures higher than 275 MPa. However, the more primitive products erupted after 27 September are amphibole-free (Ubide et al., 2023) ruling out the above reasoning. Since we used a composition erupted on the 2nd of October (i.e., amphibole-free) the lack of amphibole crystals in the experimental charges is in agreement with the observation of the amphibole-free erupted samples and its presence in the more evolved magmas should be related to other parameters rather than to the effect of the pressure. Phase relations of alkaline and tholeiitic basalts (Freise et al., 2009; Iacovino et al., 2016) show that the presence of a mixed H_2O-CO_2 fluid has the effect to increase up to ~50 °C the thermal stability of amphibole compared to its appearance in a system with a pure H_2O fluid. Recent crystallisation experiments performed under variable H_2O/CO_2 ratios for compositions erupted during the Tajogaite 2021 eruption point out that amphibole is stable up to 1065 °C (Andújar et al., 2023). We note that by expanding the stability field of amphibole by 50 °C (Fig. 2) we would be close to the maximum crystallisation temperature experimentally reproduced by Andújar (2023). Following this experimental evidence and these considerations we suggest that amphibole might have crystallised in the shallow reservoir at 275 MPa in the presence of a mixed H_2O-CO_2 fluid and that its reaction rims might have recorded its destabilization during the ascent of the magma towards the surface.

The absence of plagioclase in the experimental runs is in agreement with observations of natural samples, where it is present as a

476 microcryst phase in the matrix (Castro and Feisel 2022; Day et al., 2022;
477 Pankhurst et al., 2022; Romero et al., 2022), suggesting that plagioclase
478 nucleated and grew during magma ascent in the volcanic conduit and/or
479 during cooling of the lava outside the vent. In general, the textures and
480 chemical compositions observed in the experimental charges are in good
481 agreement with those of the natural samples.

482 Regarding the residual glass (Fig. 3), we note that the SiO_2
483 contents of the anhydrous experimental glasses and of those with 1 and
484 3 wt% H_2O added match the SiO_2 contents of the natural glasses at
485 temperatures between 1100 and 1125 °C. For the same range of
486 temperature, the experimental glasses with up 1 wt% H_2O added have
487 Al_2O_3 contents which correspond to natural glass compositions. All
488 experimental melts obtained at 1100 °C or at a higher temperature
489 replicate the CaO contents of the natural glasses. The best match for the
490 MgO content of natural glasses is found within the range 1035-1125 ˚C
491 and 1000-1114 °C, respectively, for charges with 1 and 5 % H_2O added.
492 The FeO content of the natural glasses is well reproduced in the
493 experiments performed at 1100-1125 °C. The TiO_2 concentrations of
494 natural glasses are in good agreement with glasses produced in
495 experiments at temperatures above 1050 °C, independent of the water
496 content. With the exception of the experimental glasses obtained with 5
497 wt% H_2O, all other glasses have MnO contents encompassing the
498 natural glass composition. The alkali contents of the natural glasses
499 show the best correspondence with experiments with up to 1 wt% H_2O.

The experimental glasses obtained at 1100 °C with up to 1 wt% H_2O have P_2O_5 contents with the closest resemblance to natural compositions.

4.2. Comparison with Rhyolite-MELTS modelling

In this section the experimental results are compared with those obtained by using the software package Rhyolite-MELTS designed for thermodynamic modelling of phase equilibria in magmatic systems (Ghiorso and Sack, 1995; Gualda et al., 2012). The thermodynamic modelling was performed for the same tephritic composition (CVLP-LF3 of Romero et al., 2022) used as the experimental starting material and for a slightly less evolved basanite (Castro and Feisel, 2022) erupted in November during the 2021 Cumbre Vieja eruption. To perform simulations which include the experimental conditions and also expand the T-H_2O-fO_2 space, simulations were performed for both compositions between 900-1300 °C and 0.1 and 800 MPa, for water contents of 0, 1, 3 and 5 wt% and at fO_2 values corresponding to the Nickel-Nickel Oxide (NNO) buffer -0.7 and +1.5. The oxygen fugacities in the natural system, estimated by the V-in-olivine oxybarometry technique (e.g. Wang et al., 2019), were calculated to be between NNO + 0.6 and NNO + 1.3 (Day et al., 2022).

For all simulations, spinel crystallisation was suppressed. In the parameter space investigated, the inclusion of spinel as a crystallising phase had a significant impact on the crystallisation of olivine. For the tephritic composition, Sp-bearing simulations resulted in solutions

where olivine was not found at any condition in the investigated *P*-*T*-H_2O space for a fO_2 of NNO + 1.5 and only at <10 MPa for a fO_2 equivalent to the QFM buffer (i.e., Quartz-Fayalite-Magnetite buffer equivalent to NNO – 0.7). As the experimental results at 275 MPa, fO_2 = NNO + 2 and H_2O = 0-5 wt.% demonstrate that olivine is present as a crystallising phase (Fig. 2), it is possible that the Rhyolite-MELTS underestimates olivine crystallisation when spinel is allowed to crystallise within the investigated parameter space. Instead, when spinel crystallisation is suppressed, olivine is found throughout the *P*-*T*-H_2O space. For the basanite composition, the suppression of spinel crystallisation results in a 100-150 ˚C increase in the olivine liquidus temperature, depending on the H_2O content. As the basanite composition is comparable to the tephrite, we can suggest from the results of our experiments that the Rhyolite-MELTS simulations could also underestimate the crystallisation temperature of olivine when spinel is allowed to crystallise. As olivine is also present as a phenocryst phase in the natural phase assemblage (Romero et al., 2022; Castro and Feisel, 2022; Day et al., 2022), with the crystal content increasing to 10 vol.% during later stages of the eruption (Day et al., 2022), it is important to investigate also the *P*-*T*-H_2O space of olivine crystallisation using the simulations. Therefore, for our thermodynamic modelling, we chose to exclude spinel crystallisation. For clarity, the results of Rhyolite-MELTS modelling allowing spinel crystallisation are also presented in Supplementary Figures 1 and 2 for comparison.

549 Anhydrous and hydrous simulations with 1 wt% H_2O performed
550 for the tephritic composition (Fig. 6) show the crystallisation sequence
551 clinopyroxene, olivine and plagioclase irrespective of the fO_2 conditions.
552 Those simulations with 3 wt% H_2O show the appearance of amphibole
553 only at reduced conditions for pressures higher than 300 MPa and
554 temperatures lower than 960 °C. By increasing the H_2O content to 5
555 wt% the stability field of amphibole is enlarged to include pressures
556 higher than 200 MPa and temperatures lower than 1000 °C for reducing
557 conditions and pressures higher than 400 MPa and temperatures lower
558 than 950 °C for oxidizing conditions. Increasing the H_2O content from 0
559 to 5 wt% also shifts the liquidus temperature of clinopyroxene and
560 olivine to lower temperatures by 50-60 °C. The stability field of
561 plagioclase is dramatically reduced to low pressure (<30 MPa) and low
562 temperature (<1000 ˚C) for H_2O contents of 3 and 5 wt.%. Instead,
563 plagioclase is found at higher pressure for $H_2O \leq 1$ wt.%, but still at
564 temperatures <1000 ˚C. Oxidizing conditions tend to slightly increase
565 the liquidus temperature of clinopyroxene and to decrease that of olivine.
566 At a corresponding pressure of 275 MPa the crystallisation
567 temperatures of clinopyroxene predicted by Rhyolite-MELTS are up to
568 100 °C higher than those observed in the experiments (between 1100
569 and 1125 °C). The composition of modelled olivine (at 275 MPa) ranges
570 between Fo_{79-82}, with an increase in Fo as H_2O content increases from 0
571 to 5 wt.%. For a fixed H_2O content, the Fo content decreases as
572 temperature decreases from the saturation temperature to 1000 ˚C. For
573 clinopyroxene, the modelled compositions range between $Wo_{47}En_{46}Fs_8$

574 and $Wo_{39}En_{20}Fs_{41}$, with an enrichment in the Fs component as H_2O
575 content increases. For H_2O contents between 0-1 wt.%, there is a
576 general decrease in the Wo and En components as temperature
577 decreases and a concurrent increase in Fs. However, at higher H_2O
578 contents (3-5 wt.%), Wo and En instead increase and Fs decreases
579 between the liquidus temperature and 1000 ˚C.

580 Modelled melt compositions (Supplementary Figures 3) show
581 comparable trends to the experimental results (Fig. 3), with an increase
582 in SiO_2 and alkalis and a decrease in CaO, MgO and TiO_2 with
583 decreasing temperature. The range in modelled melt chemistry for
584 simulations >1150 ˚C shows good agreement with the range in glass
585 chemistry observed in natural samples. An exception is the FeO trend,
586 where the small decrease in FeO as temperature decreases when
587 compared to the experiments is likely due to suppression of spinel
588 crystallisation in the simulations. Although there is a discrepancy with
589 the modelled liquidus temperature of the phases and that observed in the
590 experiments, the modelled phase compositions and compositional trends
591 show good agreement with the compositional range measured from both
592 natural and experimental olivine and clinopyroxene (Figs. 4, 5).

593 Therefore, while we recognize the limitations of the model,
594 particularly regarding the crystallisation of spinel, the general
595 correspondence of the phase assemblage, crystallisation sequence and
596 phase chemistry between the modelled and experimental results and
597 sample observations suggest that our combined results can provide
598 insight into the pre-eruptive condition of the Tajogaite eruption.

The less evolved basanitic composition shows model results (Fig. 7) that are substantially different from those obtained by using the tephritic composition. For the basanitic composition, the fO_2 conditions have a greater impact on crystallisation, given that at reducing conditions, the liquidus of clinopyroxene crosses that of olivine. This occurs as the liquidus of olivine is predicted to be steeper than that of clinopyroxene, and as there is a relative small difference between their predicted liquidus temperatures, compared to the larger difference predicted by the tephritic model. When the relatively low fO_2 values enlarge the stability field of olivine the clinoyroxene liquidus is crossed. At 275 MPa the crystallisation temperature of olivine predicted by Rhyolite-MELTS with 1 wt% H_2O and reducing conditions is comparable with the temperature of 1170 ˚C observed in the experiments. However, the liquidus temperature of clinopyroxene is overestimated by ~50 °C, compared to the temperature of 1160 °C observed in the experiments. Similar to the simulations performed with the tephritic composition, water has the effect of reducing the plagioclase stability field to low pressure and low temperature conditions and to stabilize the presence of amphibole, although at low temperatures (<1000 °C). Modelled olivine compositions also differ from the results of tephrite, producing a narrow range in Fo (at 275 MPa) of Fo_{85-86}. Fo content also decreases with temperature for a fixed H_2O content.

Clinopyroxene compositions vary between $Wo_{43}En_{50}Fs_{7}$ and $Wo_{31}En_{31}Fs_{39}$, showing an enrichment in the En component compared to

624 the tephritic composition. A similar trend in clinopyroxene composition
625 as a function of H_2O and temperature is observed when compared with
626 the results of the tephritic model. Modelled melt compositions for the
627 basanite composition (Supplementary Figure 4) are comparable to those
628 of the tephrite and the experimental results, with similar trends in major
629 element chemistry as a function of temperature. However, the results of
630 the basanite model have melt compositions more comparable with
631 natural glasses, particularly for Na_2O and P_2O_5.

632 The model results show that amphibole crystallisation is
633 predicted at low-temperature/high-pressure conditions (<1000 °C/>300
634 MPa). These conditions were not investigated in the experiments
635 because they are not considered to be representative of the *T-P*
636 conditions of the Tajogaite shallow reservoir.

637 The thermodynamic models also predict crystallisation of
638 plagioclase at low-temperature/low-pressure conditions (e.g., <25
639 MPa/<950 °C for the tephrite at NNO + 1.5 and 1 wt% H_2O; <25
640 MPa/<1100 °C for the basanite at 1 wt% H_2O). The more sodic
641 composition of modelled plagioclase ($An_{19-35}Ab_{59-71}Or_{4-9}$ for the
642 tephritic composition and $An_{22-67}Ab_{31-71}Or_{1-7}$ for the basanite at 1 wt%
643 H_2O) also shows better agreement with the composition of labradoritic
644 microlites than rare anorthitic phenocrysts in the natural samples
645 (Romero et al., 2022). This thermodynamic observation coupled with
646 the absence of plagioclase in the experimental charges and plagioclase
647 phenocrysts in the natural rocks suggest that plagioclase crystallisation

was restricted to magma ascent conditions within the volcanic conduit and/or during the cooling of the erupted rocks outside the vent.

4.3. Pre-eruptive conditions

Comparison between the phase equilibrium results, the thermodynamic simulations and the natural rocks allows us to constrain the temperature and water content of the magma stored in the shallow reservoir of Cumbre Vieja prior to its eruption. According to our results, the coexistence of the assemblage oxides + olivine + clinopyroxene was reproduced at 1100 °C and with H_2O contents up to 3 wt%. The skeletal and rounded-embayed shapes of olivine observed in the natural samples (Dayton et al., 2023; Day et al., 2022; Pankhurst et al., 2022) were reproduced in the experiments with up to 1 wt% H_2O added. In general, rounded-embayed crystal shapes found in natural rocks can be ascribed to dissolution processes. However, regarding experimental samples, we want to highlight that embayed olivine crystals can be generated with a small degree of undercooling (25 °C) of the system (Shea et al., 2019). Likely because when the experimental conditions are close to those required for the beginning of crystallisation of a mineral phase, small and unavoidable physical-chemical changes (e.g., temperature, water activity, oxygen fugacity) could generate a series of precipitation-dissolution cycles of unstable skeletal crystals. Following our phase diagram (Fig. 2) it is suggested that with 3 wt% water embayed olivine crystals could appear in the range 1075-1088 °C. This consideration

allows us to constrain the pre-eruptive water content of the magma to no more than 3 wt% in presence of the mineralogical assemblage olivine + clinopyroxene + oxide.

The estimated pre-eruptive temperatures in the range 1075-1088 °C (3 wt% H_2O) and around 1100 °C (1 wt% H_2O) are comparable with the measured temperatures (1100-1140 °C) of the erupted lavas just outside the vent (Carracedo et al., 2022) as well as with the high pre-eruptive temperatures (1110-1185 °C) estimated for the basanite erupted at El Hierro during 2011-2012 (Martí et al., 2013).

Moreover, the thermodynamic simulations performed for the tephritic composition at NNO + 1.5 predict compositional ranges for clinopyroxene (Wo_{39-47}) and olivine (Fo_{79-82}) in good agreement with the natural samples (Wo_{47-50}, Fo_{78-86} (Castro and Feisel, 2022; Day et al., 2022; Pankhurst et al., 2022; Romero et al., 2022)).

The absence of plagioclase in the experimental charges and their reproduction in the thermodynamic simulations at lower (<25 MPa) pressures, than the experimental ones, suggest that plagioclase crystallisation was restricted to shallower depths (<1 km) and/or to subaerial conditions during the cooling of the lava flows.

Finally, the formation of amphibole at pressures higher than 300 MPa obtained with the thermodynamic simulations and its absence in most of the experimental charges seem to suggest that its crystallisation occurred between 20 and 25 km depth (D' Auria et al., 2022; Dayton et al., 2023). In the presence of a H_2O-CO_2 mixed fluid, crystallisation of amphibole may be promoted at lower pressures than 300 MPa, but the

absence of amphibole in part of the natural samples or the presence of resorbed amphibole crystals indicate that amphibole was destabilized during magma ascent towards the surface.

5. Conclusions

The major goal of this research was to constrain the pre-eruptive water and temperature conditions of the magma stored in the shallow 2021 Tajogaite eruption reservoir at a depth of 8-12 km beneath Cumbre Vieja volcano by combining experimental phase equilibrium of erupted tephrite with thermodynamic modelling for tephritic and basanitic compositions. Our results suggest that the magma is high temperature (~1100 °C) and relatively water-rich (up to 3 wt%), that it fractionated the assemblage oxide + olivine + clinopyroxene in the shallow reservoir, and that plagioclase microlites crystallised during magma ascent towards the surface (<1 km depth) and/or outside the vent with cooling of erupted products. Further experimental works and thermodynamic simulations involving the presence of a mixed H_2O-CO_2 fluid are needed to reconcile the differences in amphibole crystallisation between the results of our experiments and simulations results and those experimental results reported in literature and to clarify the conditions of amphibole crystallisation during the Tajogaite 2021 eruption. Finally, the results presented in this work contribute to the experimental characterization of tephritic and basanitic magma and have the potential to be applicable to similar magmatic systems in hot-spot zones.

CRediT authorship contribution statement

Alessandro Fabbrizio: Conceptualization, Investigation, Writing – original draft, Writing – review & editing, Funding acquisition. **Emily C. Bamber:** Methodology, Investigation, Writing – original draft, Writing – review & editing. **Eleni Michailidou:** Investigation, Writing – review & editing, Funding acquisition. **Jorge E. Romero:** Conceptualization, Writing – review & editing, Funding acquisition. **Fabio Arzilli**: Conceptualization, Investigation, Writing – original draft, Writing – review & editing, Funding acquisition. **Barbara Bonechi:** Conceptualization, Writing – review & editing, Funding acquisition. **Margherita Polacci:** Conceptualization, Writing – review & editing, Funding acquisition. **Mike Burton:** Conceptualization, Writing – review & editing, Funding acquisition.

Acknowledgments

This research was supported by the Grant Agency of Czech Republic (GAČR, grant number 23-04734S to AF). AF and EM acknowledge support from the Grant Agency of Charles University (GAUK, project number 154123). JR is grateful to the financial support provided through NSFGEONERC-funded project DisEqm (NERC Reference: NE/N018575/1; NE/N018443/1) and V-PLUS projects for fieldwork. FA thanks the KINETICVOLC project funded by the European Union, NextGenerationEU, Ministry of University and

748 Research, Promotion and Development Fund DM737/2021. MP and BB
749 acknowledge support from the UKRI FLF project 4DVOLC
750 (MR/V023985/1). AF and EM thank M. Racek (Institute of Petrology
751 and Structural Geology, Charles University of Prague) for assistance
752 during EMPA analytical sessions. AF thanks Juan Andújar for the
753 interesting and useful discussions on the stability of amphibole. Silvio
754 Mollo and an anonymous reviewer are thanked for their constructive
755 comments and suggestions that helped to clarify the manuscript.
756

757 **References**

758

759 Andújar, J., Costa, F., Martí, J., Wolff, J.A., Carroll, M.R., 2008.
760 Experimental constraints on pre-eruptive conditions of
761 phonolitic magma from the caldera-forming El Abrigo eruption,
762 Tenerife (Canary Islands). Chem. Geol. 257, 173-194.
763 https://doi.org/10.1016/j.chemgeo.2008.08.012.
764

765 Andújar, J., Costa, F., Martí, J., 2010. Magma storage conditions of the
766 last eruption of Teide volcano (Canary Islands, Spain). Bull.
767 Volcanol. 72, 381-395. https://doi.org/10.1007/s00445-009-
768 0325-3.
769

770 Andújar, J., Costa, F., Scaillet, B., 2013. Storage conditions and eruptive
771 dynamics of central versus flank eruptions in volcanic islands:
772 The case of Tenerife (Canary Islands, Spain). J. Volcanol.

Geoth. Res. 260, 62-79. https://doi.org/10.1016/j.jvolgeores.2013.05.004.

Andújar, J., Scaillet, B., 2012. Experimental constraints on parameters controlling the difference in the eruptive dynamics of phonolitic magmas: the case of Tenerife (Canary Islands). J. Petrol. 53, 1777-1806. https://doi.org/10.1093/petrology/egs033.

Andújar, J., Scaillet, B., Di Carlo, I., Frascerra, D., Mejías, M.J., Meletlidis, M., Experimental student group from Orléans-Olot 2021-2022 course, Casillas, R., Slodczyk, A., Faranda, C.F., Núñez-Guerrero, E., Scaillet, S., 2023. Phase equilibria point to cold and shallow depth conditions for magma storage at La Palma 2021 eruption. Goldschmidt Conference, https://conf.goldschmidt.info/goldschmidt/2023/meetingapp.cgi/Paper/17945.

Arzilli, F., Agostini, C., Landi, P., Fortunati, A., Mancini, L., Carroll, M.R., 2015. Plagioclase nucleation and growth kinetics in a hydrous basaltic melt by decompression experiments. Contrib. Mineral. Petrol. 170, 55. https://doi.org/10.1007/s00410-015-1205-9.

Baker, D.R., Eggler, D.H., 1987. Compositions of anhydrous and

hydrous melts coexisting with plagioclase, augite, and olivine or low-Ca pyroxene from 1 atm to 8 kbar – Application to the Aleutian volcanic center of Atka. Am. Mineral. 72, 12-28.

Bali, E., Hartley, M.E., Halldorsson, S.A., Gudfinnsson, G.H., Jakobsson, S., 2018. Melt inclusion constraints on volatile systematics and degassing history of the 2014-2015 Holuhraun eruption, Iceland. Contrib Mineral. Petrol. 173, 9. https://doi.org/10.1007/s00410-017-1434-1.

Blundy, J., Cashman, K., 2008. Petrologic reconstruction of magmatic system variables and processes, in: Putirka, K.D., Tepley III, F.J. (Eds.), Minerals, Inclusions and Volcanic Processes. Rev. Mineral. 69, 179-239. https://doi.org/10.2138/rmg.2008.69.6.

Bonadonna, C., Pistolesi, M., Biass, S., Voloschina, M., Romero, J., Coppola, D., Folch, A., D'Auria, L., Martin-Lorenzo, A., Dominguez, L., Pastore, C., Hardy, M.P.R., Rodriguez, F., 2022. Physical characterization of long-lasting hybrid eruptions: the 2021 Tajogaite eruption of Cumbre Vieja (La Palma, Canary Islands). J. Geophys. Res. Solid 127. https://doi.org/10.1029/2022JB025302.

Carracedo, J.C., Troll, V.R., Day, J.M.D., Geiger, H., Aulinas, M., Soler,

V., Deegan, F.M., Perez-Torrado, F.J., Gisbert, G., Gazel, E., Rodriguez-Gonzalez, A., Albert, H., 2022. The 2021 eruption of the Cumbre Vieja volcanic ridge on La Palma, Canary Islands. Geol. Today 38, 82-120. https://doi.org/10.1111/gto.12388.

Caracciolo, A., Kahl, M., Bali, E., Gudfinnsson, G.H., Halldorsson, S.A., Hartley, M.E., 2021. Timescales of crystal mush mobilization in the Baroarbunga-Veioivotn volcanic system based on olivine diffusion chronometry. Am. Mineral. 106, 1083-1096. https://doi.org/10.2138/am-2021-7670.

Cas, R.A.F., Wolff, J.A., Martí, J., Olin, P.H., Edgar, C.J., Pittari, A., Simmons, J.M., 2022. Tenerife, a complex end member of basaltic oceanic island volcanoes, with explosive polygenetic phonolitic calderas, and phonolitic-basaltic stratovolcanoes. Earth-Sci. Rev. 230, 103990. https://doi.org/10.1016/j.earscirev.2022.103990.

Castro, J.M., Feisel, Y., 2022. Eruption of ultralow-viscosity basanite magma at Cumbre Vieja, La Palma, Canary Islands. Nat. Commun. 13, 3174. https://doi.org/10.1038/s41467-022030905-4.

Colle, F., Masotta, M., Costa, S., Mollo, S., Landi, P., Pontesilli, A.,

Peres, S., Mancini, L., 2023. Effect of undercooling on clinopyroxene crystallization in a high K basalt: Implications for magma dynamics at Stromboli volcano. Lithos (in press), 107327. https://doi.org/10.1016/j.lithos.2023.107327.

D'Auria, L., Koulakov, I., Prudencio, J., Cabrera-Pérez, I., Ibáñez, J.M., Barrancos, J., García-Hernández, R., Martínez van Dorth, D., Padilla, G.D., Przeor, M., Ortega, V., Hernández, P., Peréz, N.M., 2022. Rapid magma ascent beneath La Palma revealed by seismic tomography. Sci. Rep. 12, 17654. https://doi.org/10.1038/s41598-022-21818-9.

Day, J.M.D., Troll, V.R., Aulinas, M., Deegan, F.M., Geiger, H., Carracedo, J.C., Pinto, G.G., Perez-Torrado, F.J., 2022. Mantle source characteristics and magmatic processes during the 2021 La Palma eruption. Earth Planet. Sci. Lett. 597, 117793. https://doi.org/10.1016/j.epsl.2022.117793.

Dayton, K., Gazel, E., Wieser, P., Troll, V.R., Varracedo, J.C., La Madrid, H., Roman, D.C., Ward, J., Aulinas, M., Geiger, H., Deegan, F.M., Gisbert, G., Perez-Torrado, F.J., 2023. Deep magma storage during the 2021 La Palma eruption. Sci. Adv. 9, eade7641. https://doi.org/10.1126/sciadv.ade7641.

Di Fiore, F., Vona, A., Scarani, A., Giordano, G., Romano, C., Giordano,

D., Caricchi, L., Lorenzo, A.M., Rodriguez, F., Coldwell, B., Hernandez, P., Pankhurst, M., 2023. Experimental constraints of the rheology of lavas from 2021 Cumbre Vieja eruption (La Palma, Spain). Geophys. Res. Lett. 50, e2022GL100970. https://doi.org/10.1029/2022GL100970.

Fabbrizio, A., Rouse, P.J., Carroll, M.R., 2006. New experimental data on biotite + magnetite + sanidine saturated phonolitic melts and application to the estimation of magmatic water fugacity. Am. Mineral. 91, 1863-1870. https://doi.org/10.2138/am.2006.2055.

Fabbrizio, A., Schmidt, M.W., Petrelli, M., 2021. Effect of fO_2 on Eu partitioning between clinopyroxene, orthopyroxene and basaltic melt: Development of a Eu^{3+}/Eu^{2+} oxybarometer. Chem. Geol 559, 119967. https://doi.org/10.1016/j.chemgeo.2020.119967.

Faure, F., Trolliard, G., Nicollet, C., Montel, J.M., 2003. A developmental model of olivine morphology as a function of the cooling rate and the degree of undercooling. Contrib. Mineral. Petrol. 145, 251-263. https://doi.org/10.1007/s00410-003-0449-y.

Faure, F., Schiano, P., Trolliard, G., Nicollet, C., Soulestin, B., 2007.

Textural evolution of polyhedral olivine experiencing rapid cooling rates. Contrib. Mineral. Petrol. 153, 405-416. https://doi.org/10.1007/s00410-006-0154-8.

Freise, M., Holtz, F., Nowak, M., Scoates, J.S., Strauss, H., 2009. Differentiation and crystallization conditions of basalts from the Kerguelen large igneous province: an experimental study. Contrib. Mineral. Petrol. 158, 505-527. https://doi.org/10.1007/s00410-009-0394-5.

Ghiorso, M.S., Sack, R.O., 1995. Chemical mass-transfer in magmatic processes .4. A revised and internally consistent thermodynamic model for the interpolation and extrapolation of liquid-solid equilibria in magmatic systems at elevated-temperatures and pressures. Contrib. Mineral. Petrol. 119, 197-212. https://doi.org/10.1007/BF00307281.

Gualda, G.A.R., Ghiorso, M.S., Lemons, R.V., Carley, T.L., 2012. Rhyolite-MELTS: a modified calibration of MELTS optimized for silica-rich, fluid-bearing magmatic systems. J. Petrol. 53, 875-890. https://doi.org/10.1093/petrology/egr080.

Haddadi, B., Sigmarsson, O., Larsen, G., 2017. Magma storage beneath Grimsvotn volcano, Iceland, constrained by clinopyroxene-melt thermobarometry and volatiles in melts inclusions and

groundmass glass. J. Geophys. Res. Solid 122, 6984-6997. https://doi.org/10.1002/2017JB014067.

Hartley, M.E., Bai, E., Maclennan, J., Neave, D.A., Halldorsson, S.A., 2018. Melt inclusion constraints on petrogenesis of the 2014-2015 Holuhraun eruption, Iceland. Contrib. Mineral. Petrol. 173, 10. https://doi.org/10.100/s00410-017-1435-0.

Hildner, E., Klugel, A., Hansteen, T.H., 2012. Barometry of lavas from the 1951eruption of Fogo, Cape Verde Islands: Implications for historic and prehistoric magma plumbing systems. J. Volcanol. Geotherm. Res. 217, 73-90. https://doi.org/10.1016/j.jvolgeores.2011.12.014.

Houghton, B.F., Gonnermann, H.M., 2008. Basaltic explosive volcanism: Constraints from deposits and models. Geochem. 68, 117-140. https://doi.org/10.1016/j.chemer.2008.04.002.

Hughes, E.C., Buse, B., Kearns, S.L., Blundy, J.D., Kilgour, G., Mader, H.M., 2019. Low analytical totals in EPMA of hydrous silicate glass due to sub-surface charging: Obtaining accurate volatiles by difference. Chem. Geol. 505, 48-56. https://doi.org/10.1016/chem.geo.2018.11.015.

Iacovino, K., Oppenheimer, C., Scaillet, B., Kyle, P., 2016. Storage and

evolution of mafic and intermediate alkaline magmas beneath Ross Island, Antarctica. J. Petrol. 57, 93-118. https://doi.org?10.1093/petrology/egv083.

Kirkpatrick, J.R., 1981. Kinetics of crystallization of igneous rocks, in: Lasaga, A.C., Kirkpatrick, J.R. (Eds.), Kinetics of Geochemical Processes. Rev. Mineral. Geochem. 8, 321-398.

Klugel, A., Hansteen, T.H., Galipp, K., 2005. Magma storage and underplating beneath Cumbre Vieja Volcano, La Palma (Canary Islands). Earth Planet. Sci. Lett. 236, 211-226. https://doi.org/10.1016/j.epsl.2005.04.006.

Kovalenko, V.I., Naumov, V.B., Girnis, A.V., Dorofeeva, V.A., Yarmolyuk, V.V., 2007. Volatiles in basaltic magmas of ocean islands and their mantle sources: I. Melt compositions deuced from melt inclusions and glasses in the rocks. Geochem. Int. 45, 105-122. https://doi.org/10.1134/S0016702907020012.

Lang, S., Mollo, S., France, L., Misiti, V., Nazzari, M., 2021. Kinetic partitioning of major-minor cations between olivine and Hawaiian tholeiitic basalt under variable undercooling and cooling rate conditions. Chem. Geol. 584, 120485. https://doi.org/10.1016/j.chemgeo.2021.120485.

La Spina, G., Burton, M., Vitturi, M.D., Arzilli, F., 2016. Role of syn-eruptive plagioclase disequilibrium crystallization in basaltic magma ascent dynamics. Nat. Commun. 7, 13402. https://doi.org/10.1038/ncomms13402.

Longpré, M.-A., Stix, J., Klügel, A., Shimizu, N., 2017. Mantle to surface degassing of carbon- and sulphur-rich alkaline magma at El Hierro, Canary Islands. Earth Planet. Sci. Lett. 460, 268-280. https://doi.org/10.1016/j.epsl.2016.11.043.

MacDonald, A., Ubide, T., Mollo, S., Masotta, M., Pontesilli, A., 2022. Trace element partitioning in zoned clinopyroxene as a proxy for undercooling: Experimental constraints from trachybasaltic magmas. Geochim. Cosmochim. Acta 336, 249-268. https://doi.org/10.1016/j.gca.2022.09.007.

Martí, J., Castro, A., Rodríguez, C., Costa, F., Carrasquilla, S., Pedreira, R., Bolos, X., 2013. Correlation of magma evolution and geophysical monitoring during the 2011-2012 El Hierro (Canary Islands) submarine eruption. J. Petrol. 54, 1349-1373. https://doi.org/10.1093/petrology/egt014.

Martínez-Martínez, J., Mediato, J.F., Mata, M.P., Ordóñez, B., del Moral, B., Bellido, E., Pérez-López, R., Rodríguez-Pascua, M.A., Vegas, J., Lozano Otero, G., Mateos, R.M., Sánchez, N.,

Galindo, I., 2023. Early fumarolic minerals from the Tajogaite volcanic eruption (La Palma 2021). J. Volcanol. Geotherm. Res. 435, 107771. https://doi.org/10.1016/j.jvolgeores.2023.107771.

Masotta, M., Freda, C., Gaeta, M., 2012. Origin of crystal-poor, differentiated magmas: insights from thermal gradient experiments. Contrib. Mineral. Petrol. 163, 49-65. https://doi.org/10.1007/s00410-011-0658-8.

Masotta, M., Pontesilli, A., Mollo, S., Armienti, P., Ubide, T., Nazzari, M., Scarlato, P., 2020. The role of undercooling during clinopyroxene growth in trachybasaltic magmas: Insights on magma decompression and cooling at Mt. Etna volcano. Geochim. Cosmochim. Acta 268, 258-276. https://doi.org/10.1016/j.gca.2019.10.009.

Moschini, P., Mollo, S., Gaeta, M., Fanara, S., Nazzari, M., Petrone, C.M., Scarlato, P., 2021. Parameterization of clinopyroxene growth kinetics via crystal size distribution (CSD) analysis: Insights into the temporal scales of magma dynamics at Mt. Etna volcano. Lithos 396, 106225. https://doi.org/10.1016/j.lithos.2021.106225.

Oglialoro, E., Frezzotti, M.L., Ferrando, S., Tiraboschi, C., Principe, C.,

Groppelli, G.,Villa, I.M., 2017. Lithospheric magma dynamics beneath the El Hierro Volcano, Canary Islands: insights from fluid inclusions. Bull. Volcanol. 79, 70. https://doi.org/10.1007/s00445-017-1152-6.

Padron, E., Perez, N.M., Hernandez, P.A., Sumino, H., Melian, G.V., Alonso, M., Rodriguez, F., Asensio-Ramos, M., D'Auria, L., 2022. Early precursory changes in the He-3/He-4 ratio prior to the 2021 Tajogaite eruption at Cumbre Vieja Volcano, La Palma, Canary Islands. Geophys. Res. Lett. 49, e2022GL099992. https://doi.org/10.1029/2022GL099992.

Pankhurst, M.J., Scarrow, J.H., Barbee, O.A., Hickey, J., Coldwell, B.C., Rollinson, G.K., Rodríguez-Losada, J.A., Martín-Lorenzo, A., Rodríguez, F., Hernández, W., Calvo Fernández, D., Hernández, P.A., Pérez, N.M., 2022. Rapid response petrology for the opening eruptive phase of the 2021 Cumbre Vieja eruption, La Palma, Canary Islands. Volcanica 5(1), 1-10. https://doi.org/10.30909/vol.05.01.0110.

PEVOLCA, 2021. Plan Especial de Protección Civil y Atención de Emergencias por riesgo volcánico en la Comunidad Autónoma de Canarias. https://info.igme.es/eventos/Erupcion-volcanica-la-palma/pevolca (accessed 10 July 2023).

Polacci, M., Arzilli, F., La Spina, G., Le Gall, N., Cai, B., Hartley, M.E., Di Genova, D., Vo, N.T., Nonni, S., Atwood, R.C., Llewellin, E.W., Lee, P.D., Burton, M.R., 2018. Crystallisation in basaltic magmas revealed via in situ 4D synchrotron X-ray microtomography. Sci. Rep. 8, 8377. https://doi.org/10.1038/s41598-018-26644-6.

Romero, J.E., Burton, M., Caceres, F., Taddeucci, J., Civico, R., Ricci, T., Pankhurst, M.J., Hernandez, P.A., Bonadonna, C., Llewellin, E.W., Pistolesi, M., Polacci, M., Solana, C., D'Auria, L., Arzilli, F., Andronico, D., Rodriguez, F., Asensio-Ramos, M., Martin-Lorenzo, A., Hayer, C., Scarlato, P., Perez, N.M., 2022. The initial phase of the 2021 Cumbre Vieja ridge eruption (Canary Islands): products and dynamics controlling edifice growth and collapse. J. Volcanol. Geotherm. Res. 431, 107642. https://doi.org/10.1016/j.jvolgeores.2022.107642.

Shea, T., Hammer, J.E., Helleband, E., Mourey, A.J., Costa, F., First, E.C., Lynn, K.J., Melnik, O., 2019. Phosphorus and aluminum zoning in olivine: contrasting behavior of two nominally incompatible trace elements. Contrib. Mineral. Petrol. 174, 95. https://doi.org/10.1007/s00410-019-1639-6.

Taracsák, Z., Hartley, M.E., Burgess, R., Edmonds, M., Iddon, F.,

Longpré, M.-A., 2019. High fluxes of deep volatiles from ocean island volcanoes: Insights from El Hierro, Canary Islands. Geochim. Cosmochim. Acta 258, 19-36. https://doi.org/10.1016/j.gca.2019.05.020.

Ubide, T., Márquez, Á., Ancochea, E., Huertas, M.J., Herrera, R., Coello-Bravo, J.J., Sanz-Mangas, D., Mulder, J., MacDonald, A., Galindo, I., 2023. Discrete magma injections drive the 2021 La Palma eruption. Sci. Adv. 9, eadg4813. https://doi.org/10.1126/sciadv.adg4813.

Walowski, K.J., Kirstein, L.A., De Hoog, J.C.M., Elliott, T.R., Savov, I.P., Jones, R.E., 2019. Investigating ocean island mantle source heterogeneity with boron isotopes in melt inclusions. Earth Planet. Sci. Lett. 508, 97-108. https://doi.org/10.1016/j.epsl.2018.12.005.

Wang, J., Xiong, X., Takahashi, E., Zhang, L., Li, L., Liu, X., 2019. Oxidation state of arc mantle revealed by partitioning of V, Sc and Ti between mantle minerals and basaltic melts. J. Geophys. Res., Solid Earth 124, 4617-4638. https://doi.org/10.1029/2018JB016731.

Weis, F.A., Skogby, H., Troll, V.R., Deegan, F.M., Dahren, B., 2015.

Magmatic water contents determined through clinopyroxene: Examples from the Western Canary Islands, Spain. Geochem. Geophys. Geosystems 16, 2127-2146. https://doi.org/10.1002/2015GC005800.

Figure and Table Captions

Fig. 1. BSE images of selected experimental runs. (a) Crystallisation run at 1100 °C/1 wt% H_2O: euhedral clinopyroxene (Cpx) with sectors enriched in Si-Mg (darker sectors) and in Ti-Al (brighter sectors), skeletal olivine (Ol) with embayements and melt pockets, and euhedral chromium spinel (Cr-spinel). (b) Crystallisation run at 1125 °C/1 wt% H_2O: euhedral olivine and chromium spinel. (c) Reversal experiment at 1100 °C/1 wt% H_2O with a run duration of 48 hours: euhedral clinopyroxene, euhedral olivine with melt pocket and olivine with embayements, euhedral chromium spinel. (d) Reversal experiment with 1 wt% H_2O added heated directly from room temperature to 1100 °C: euhedral clinopyroxene with sectors enriched in Si-Mg (darker sectors) and in Ti-Al (brighter sectors), euhedral olivine and chromium spinel. The bright zone around the experimental charges in (a), (b) and (c) is the $Au_{80}Pd_{20}$ capsule. Scale bar length is 100 μm in all pictures.

Fig. 2. Phase diagram showing the stability fields of mineral phases as a

function of experimental temperature and added water. Closed circles: crystallisation experiments. Arrows: reversal experiments. Cr-sp: chromium spinel; Ol: olivine; Cpx: clinopyroxene; Ti-mt: titanium magnetite; Amph: amphibole; Ap: apatite.

Fig. 3. Variations of oxide concentrations (a-l), recalculated to 100 wt% anhydrous, of the residual melts as a function of experimental temperature. The black circle shows the bulk-rock composition of the natural tephrite (CVLP-LF3; Romero et al., 2022). The dotted horizontal lines shows the minimal and maximal oxide concentrations in natural glasses (Castro and Feisel 2022; Romero et al., 2022; Dayton et al., 2023). The vertical dashed lines show the crystallisation temperature of clinopyroxene (Cpx) and apatite (Ap). (a) SiO_2; (b) Al_2O_3; (c) CaO; (d) MgO; (e) FeO; (f) TiO_2; (g) MnO; (h) Na_2O; (i) K_2O; (l) P_2O_5. If not shown error bars are smaller than symbols.

Fig. 4. (a) Compositional variations for olivine (olivine Fo%) and (b) for clinopyroxene (pyroxene Wo%) as a function of experimental temperature. The dotted horizontal lines shows the minimal and maximal amount of forsterite and wollastonite in natural olivine and clinopyroxene (Castro and Feisel 2022; Day et al., 2022; Pankhurst et al., 2022; Romero et al., 2022; Dayton et al., 2023).

Fig. 5. Ternary classification diagram for pyroxene showing the experimental (diamonds) and natural (circles) compositions.

Fig. 6. Results of Rhyolite-MELTS simulations (a-h), showing phase diagrams for the tephritic (CVLP-LF3) melt composition as a function of H_2O content and fO_2. (a) fO_2 = NNO + 1.5, H_2O = 0 wt%; (b) fO_2 = QFM, H_2O = 0 wt%; (c) fO_2 = NNO + 1.5, H_2O = 1 wt%; (d) fO_2 = QFM, H_2O = 1 wt%; (e) fO_2 = NNO + 1.5, H_2O = 3 wt%; (f) fO_2 = QFM, H_2O = 3 wt%; (g) fO_2 = NNO + 1.5, H_2O = 5 wt%; (h) fO_2 = QFM, H_2O = 5 wt%. Cpx: clinopyroxene; Ol: olivine; Plg: plagioclase; Hbl: Hornblende.

Fig. 7. Results of Rhyolite-MELTS simulations (a-h), showing phase diagrams for the basanite melt composition as a function of H_2O content and fO_2. (a) fO_2 = NNO + 1.5, H_2O = 0 wt%; (b) fO_2 = QFM, H_2O = 0 wt%; (c) fO_2 = NNO + 1.5, H_2O = 1 wt%; (d) fO_2 = QFM, H_2O = 1 wt%; (e) fO_2 = NNO + 1.5, H_2O = 3 wt%; (f) fO_2 = QFM, H_2O = 3 wt%; (g) fO_2 = NNO + 1.5, H_2O = 5 wt%; (h) fO_2 = QFM, H_2O = 5 wt%. Cpx: clinopyroxene; Ol: olivine; Plg: plagioclase; Hbl: Hornblende.

Table 1 Starting material compositions.

Table 2 Experimental conditions at 275 MPa and phase assemblage.

Supplementary Table 1 EMPA analyses for the synthesized phases and BSE images of the experimental charges.

Supplementary Fig. 1 Results of Rhyolite-MELTS simulations (a-h), considering spinel crystallisation, showing phase diagrams for the tephritic (CVLP-LF3) melt composition as a function of H_2O content and fO_2. (a) fO_2 = NNO + 1.5, H_2O = 0 wt%; (b) fO_2 = QFM, H_2O = 0 wt%; (c) fO_2 = NNO + 1.5, H_2O = 1 wt%; (d) fO_2 = QFM, H_2O = 1 wt%; (e) fO_2 = NNO + 1.5, H_2O = 3 wt%; (f) fO_2 = QFM, H_2O = 3 wt%; (g) fO_2 = NNO + 1.5, H_2O = 5 wt%; (h) fO_2 = QFM, H_2O = 5 wt%.

Supplementary Fig. 2 Results of Rhyolite-MELTS simulations (a-h), considering spinel crystallisation, showing phase diagrams for the basanite melt composition as a function of H_2O content and fO_2. (a) fO_2 = NNO + 1.5, H_2O = 0 wt%; (b) fO_2 = QFM, H_2O = 0 wt%; (c) fO_2 = NNO + 1.5, H_2O = 1 wt%; (d) fO_2 = QFM, H_2O = 1 wt%; (e) fO_2 = NNO + 1.5, H_2O = 3 wt%; (f) fO_2 = QFM, H_2O = 3 wt%; (g) fO_2 = NNO + 1.5, H_2O = 5 wt%; (h) fO_2 = QFM, H_2O = 5 wt%.

Supplementary Fig. 3 Modelled melt compositions for the tephritic starting composition CVLP-LF3 at a pressure of 275 MPa and fO_2 = NNO+1.5.

Supplementary Fig. 4 Modelled melt compositions for the basanitic composition at a pressure of 275 MPa and fO_2 = NNO+1.5.

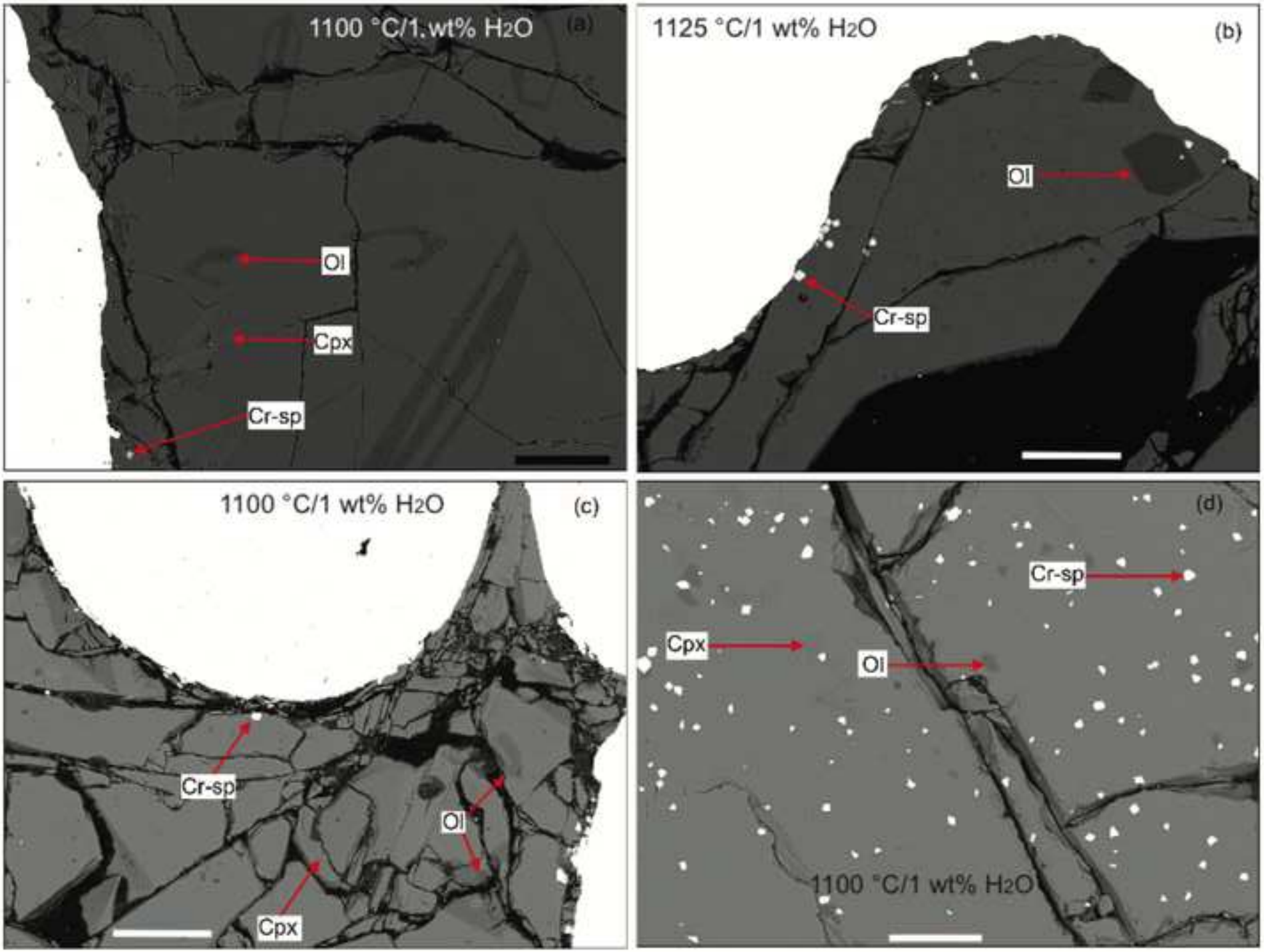

Figure_2_single_column

Click here to access/download;Figure;Figure 2_single_column.tif

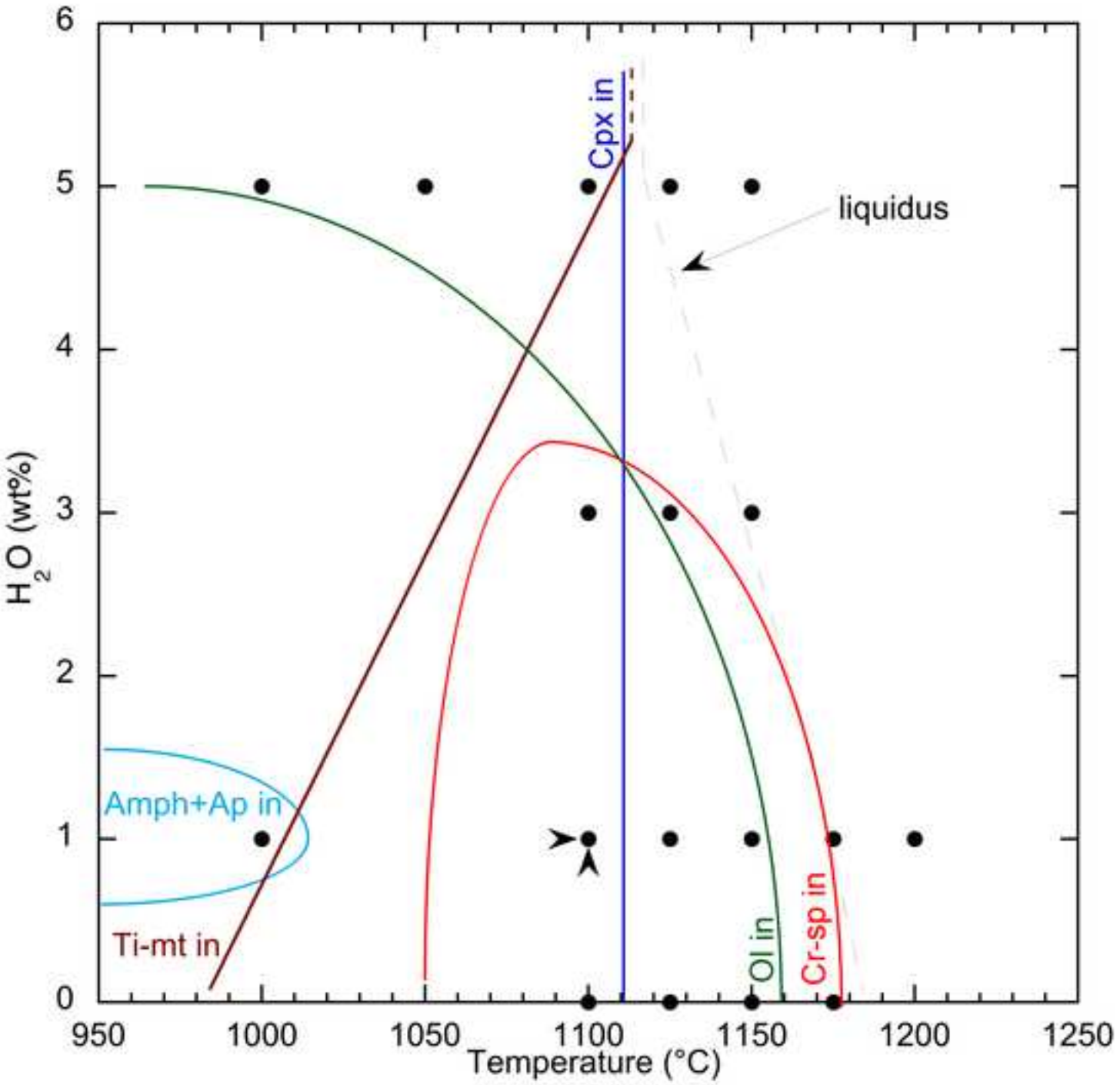

Figure_3_oneandhalf_column

Click here to access/download;Figure;Figure 3_oneandhalfcolumn.tif

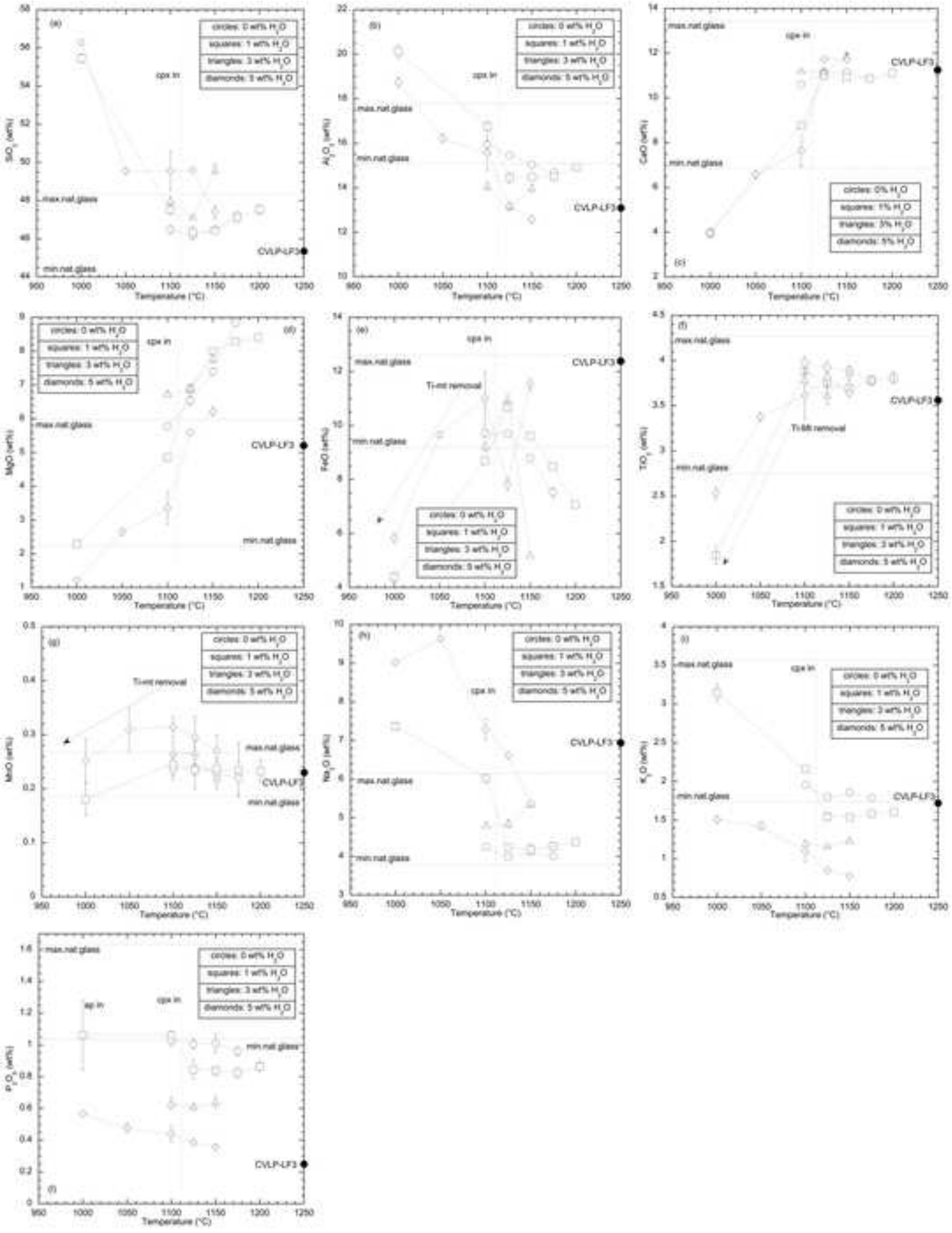

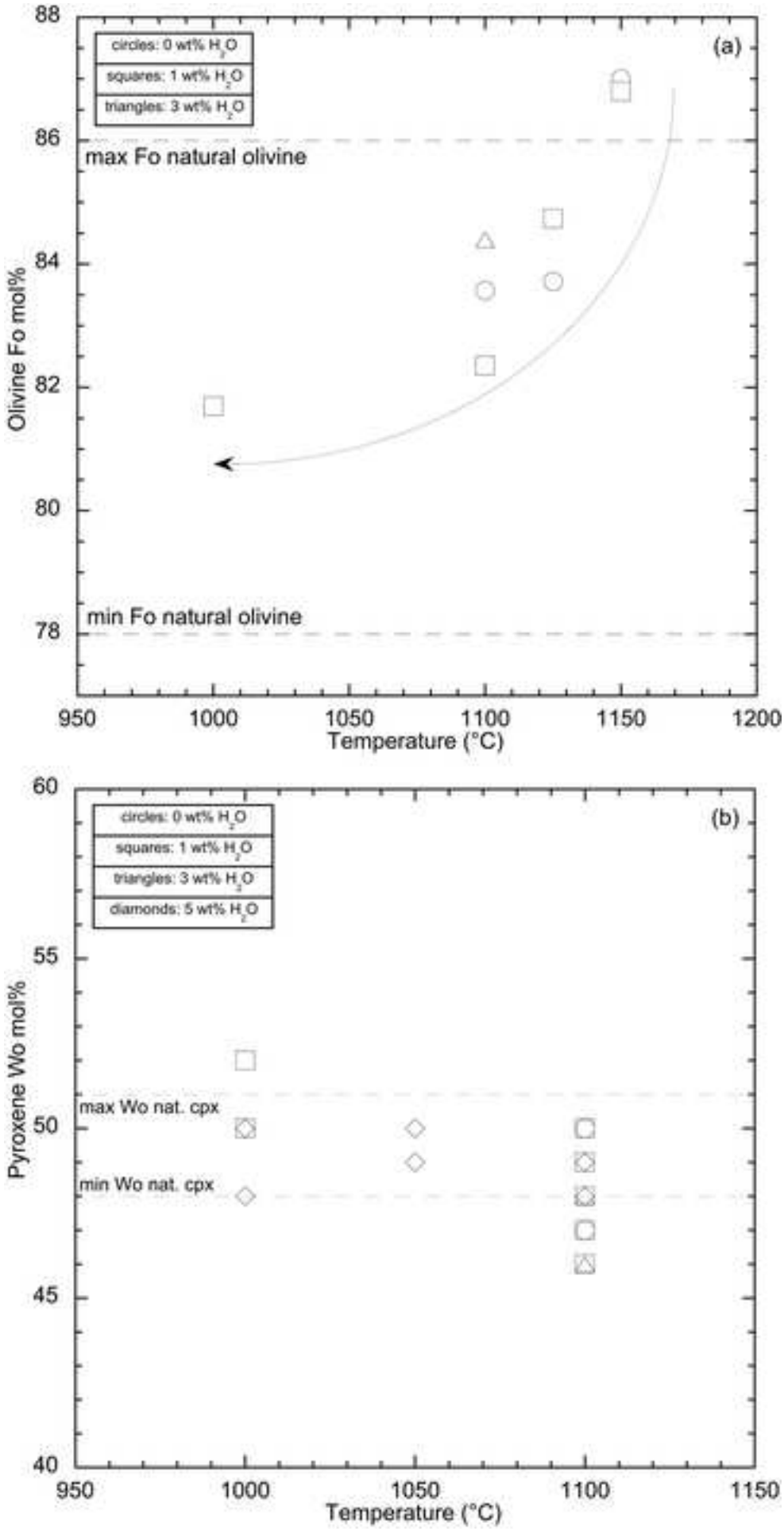

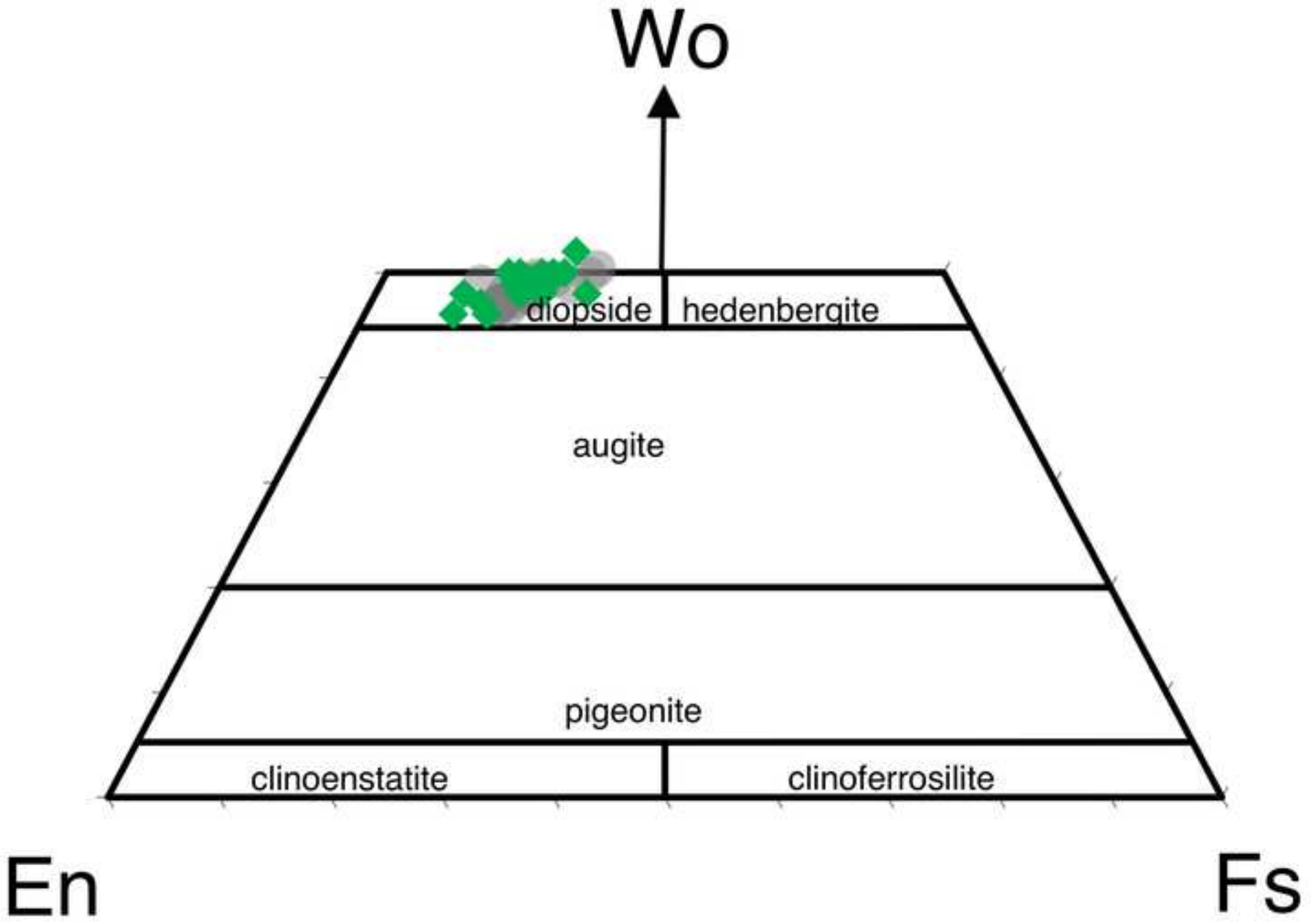

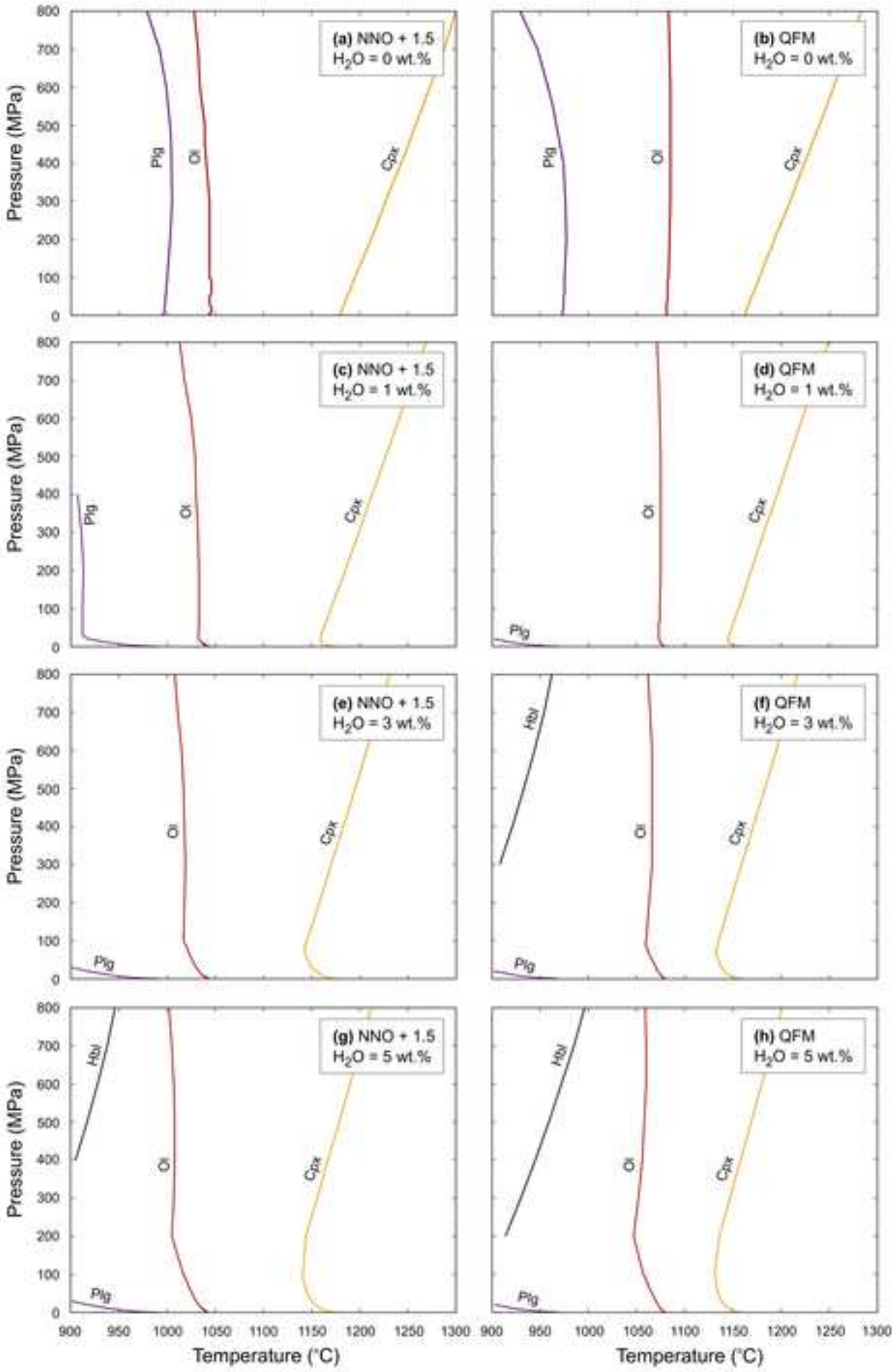

Figure_7_single_column

Click here to access/download;Figure;Figure 7_single_column.tif

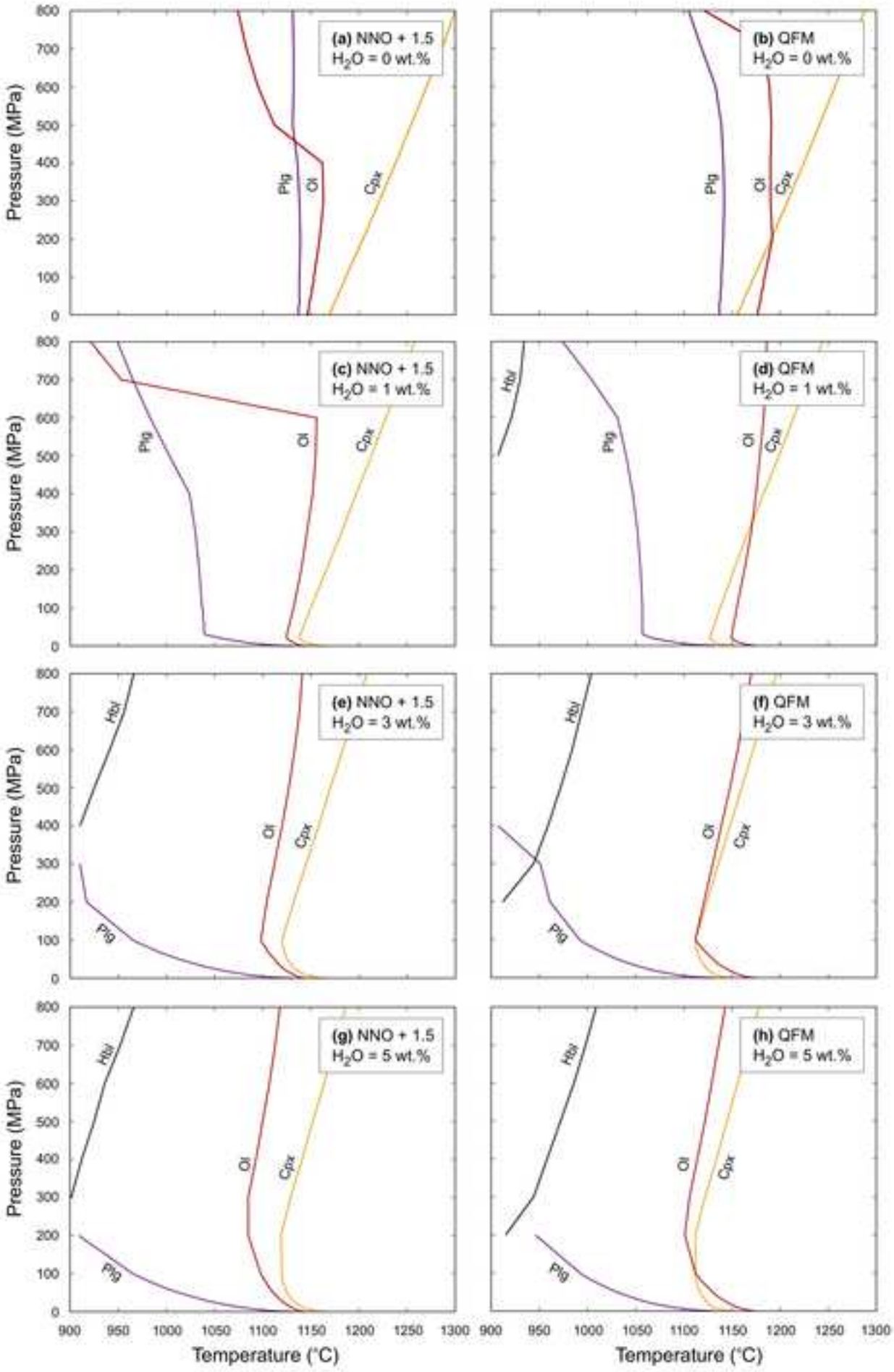

Table 1
Starting material compositions.

	CVLP-LF3	CVLP-LF3-5%	CVLP-LF3-3%	CVLP-LF3-1%
SiO_2 (wt%)	44.90	42.75	43.61	44.47
TiO_2	3.51	3.36	3.42	3.48
Al_2O_3	12.98	12.37	12.61	12.86
FeO	12.26	11.67	11.90	12.14
MnO	0.23	0.24	0.24	0.23
MgO	5.16	4.91	5.01	5.11
CaO	11.15	10.60	10.82	11.04
Na_2O	6.87	6.54	6.67	6.80
K_2O	1.71	1.62	1.66	1.69
P_2O_5	0.25	0.24	0.24	0.25
H_2O[a]	-	4.71	2.83	0.94
TrE[b]	0.99	0.99	0.99	0.99
Total	100.00	100.00	100.00	100.00

The composition of CVLP-LF3 is the natural lava composition (Romero et al. 2022) recalculated to 100% after the addition of 1 wt% trace elements.
The CVLP-LF3-5% composition is the hydrous-rich synthetic composition, analogue to the natural CVLP-LF3, recalculated to 100% after the addition of 5 wt% water and of 1 wt% trace elements.
The CVLP-LF-3% and CVLP-LF3-1% compositions were obtained by mixing the CVLP-LF3 and CVLP-LF3-5% compositions in the ratio 40:60 and 80:20, respectively.
[a]H_2O added as $Al(OH)_3$, see text.
[b]TrE: trace elements